PHYSICAL REVIEW D **95,** 094508 (2017)

Deconfinement, gradient, and cooling scales for pure SU(2) lattice gauge theory

Bernd A. Berg and David A. Clarke

Department of Physics, Florida State University, Tallahassee, Florida 32306-4350, USA

(Received 28 December 2016; published 18 May 2017)

We investigate the approach of pure SU(2) lattice gauge theory with the Wilson action to its continuum limit using the deconfining phase transition, the gradient flow and the cooling flow to set the scale. For the gradient and cooling scales we explore three different energy observables and two distinct reference values for the flow time. When the aim is to follow scaling towards the continuum limit, one gains at least a factor of 100 in computational efficiency by relying on the gradient instead of the deconfinement scale. Using cooling instead of the gradient flow one gains another factor of at least 34 in computational efficiency on the gradient flow part without any significant loss in the accuracy of scale setting. Concerning our observables, the message is to keep it simple. The Wilson action itself performs as well as or even better than the other two observables explored. Two distinct fitting forms for scaling are compared, of which one connects to asymptotic scaling. Differences of the obtained estimates show that systematic errors of length ratios, though only about 1%, can be considerably larger than statistical errors of the same observables.

DOI: 10.1103/PhysRevD.95.094508

I. INTRODUCTION

Nowadays lattice gauge theory (LGT) calculations, for instance for the QCD spectrum, come close to aiming at an accuracy of about 1% [1]. Therefore, it appears to us desirable to check a model that allows rather easily for large statistics for the accuracy that can be obtained there.

We consider pure SU(2) LGT with the Wilson action

$$S = \beta \sum_{n,\mu<\nu} \left(1 - \frac{1}{2}\mathrm{Tr} U^{\square}_{\mu\nu}(n)\right), \qquad \beta = 4/g_0^2, \quad (1)$$

$$U^{\square}_{\mu\nu}(n) = U_\mu(n) U_\nu(n+\hat{\mu}) U^{\dagger}_\mu(n+\hat{\nu}) U^{\dagger}_\nu(n). \quad (2)$$

Here $\hat{\mu}$, $\hat{\nu}$ are unit vectors in positive μ, $\nu = 1, 2, 3, 4$ directions; $U^{\square}_{\mu\nu}$ is the product of SU(2) link variables along the boundary of a plaquette with one corner at site $n = (n_1, n_2, n_3, n_4)$; and g_0 is the bare coupling.

Due to its computational simplicity, pure SU(2) LGT is well suited as a showcase for computational methodology. Computational pitfalls or shortcomings are more easily identifiable than in more complex systems like QCD. Furthermore, with modest CPU time resources, pure SU(2) LGT allows one to study the approach to the continuum limit for an entire range of suitable coupling constant values and lattice sizes. We investigate the approach of SU(2) LGT to its continuum limit using three different methods to set the scale:

(1) The deconfining phase transition [2]. The deconfinement length scale is set by the inverse transition temperature times the lattice spacing a. It has no ambiguities in its definition, but one needs to fit a number of parameters. Calculations of transition temperatures become very CPU time demanding with increasing lattice size.

(2) Lüscher's gradient flow [3]. When defining the gradient scale one encounters a number of ambiguities. Once they are fixed, there are no parameters to fit. In our calculations the CPU time demands are reduced by at least 2 orders of magnitude when compared with the deconfinement scale.

(3) Bonati and D'Elia [4] noted that similar results as with the gradient scale are even more efficiently obtained using cooling [5] instead of the gradient flow. We demonstrate here in quantitative detail that the cooling and gradient scales are for practical purposes equivalent. One gains another factor of at least 34 in computational efficiency on the gradient flow part by using cooling instead.

Our results are obtained by Markov chain Monte Carlo (MCMC) simulations for which we report the statistics in units of Monte Carlo plus overrelaxation (MCOR) sweeps. One MCOR sweep updates each link once in a systematic order [6] with the Fabricius-Haan-Kennedy-Pendleton [7] heatbath algorithm and, in the same systematic order, twice by overrelaxation [8]. Using checkerboard coding [9] and MPI Fortran, parallel updating of sublattices is implemented, and our SU(2) code is a scaled-down version of the SU(3) code documented in Ref. [10].

In the next section our estimates for the SU(2) deconfining phase transition are reported. Section III presents our results for six SU(2) gradient scales. In Sec. IV the gradient flow is replaced by cooling. We analyze scaling and asymptotic scaling in Sec. V. Summary and conclusions are given in the final section, Sec. VI.

II. DECONFINEMENT SCALE

We perform MCMC simulations on $N_s^3 N_\tau$ lattices and estimate critical coupling constants $\beta_c(N_\tau)$ up to $N_\tau = 12$ by three-parameter fits

$$\beta_c(N_s, N_\tau) = \beta_c(N_\tau) + a_1(N_\tau) N_s^{a_2(N_\tau)} \tag{3}$$

of pseudocritical $\beta_c(N_s, N_\tau)$ values, where the fit parameters $\beta_c(N_\tau)$ estimate the infinite volume values $\beta_c(N_s, \infty)$. Inverting the results of these fits defines the deconfining length scale

$$N_\tau(\beta_c) \tag{4}$$

to which we attach error bars by means of the equation

$$\triangle N_\tau = \frac{N_\tau}{L_{10}^{1,3}(\beta_c)} [L_{10}^{1,3}(\beta_c) + L_{10}^{1,3}(\beta_c - \triangle\beta_c)], \tag{5}$$

where the length scale $L_{10}^{1,3}(\beta)$ is introduced later in the paper (N_τ error bars depend only mildly on the choice of the interpolation of its scaling behavior).

We use the locations of maxima of the Polyakov susceptibility to define pseudocritical $\beta_c(N_s, N_\tau)$ values. Polyakov loops $P_{\vec{x}}$ are products of SU(2) matrices along straight lines in the N_τ direction. The argument $\vec{x}$ labels their locations on the spatial N_s^3 sublattice. From the sum over all Polyakov loops $P = \sum_{\vec{x}} P_{\vec{x}}$ one finds the susceptibility

$$\chi(\beta) = \frac{1}{N_s^3} [\langle P^2 \rangle - \langle |P| \rangle^2], \tag{6}$$

which is the analogue to the magnetic susceptibility of a spin system in three dimensions. We also implemented measurements of the thermal Polyakov loop susceptibility

$$\chi_T(\beta) = \frac{1}{N_s^3} \frac{d}{d\beta} \langle |P| \rangle, \tag{7}$$

but maxima are less pronounced than for $\chi(\beta)$.

We use reweighting in small neighborhoods of the simulation points to extract pseudocritical β values from the locations of the maxima. The error bars are then estimated by repeating the entire procedure for ≥ 32 jackknife bins (see, e.g., [6]). Notably, the estimates of pseudocritical β values from the maxima of (6) and (7) may not fall into one reweighting range, though they have ultimately identical $N_s \to \infty$ limits. So, to reduce computational requirements one is pressed to make a decision in favor of one of them.

Together with their goodness of fit q (for the definition see, e.g., Ref. [6]), our pseudocritical β_c estimates are compiled in Tables I and II. In previous literature Engels *et al.* [11] studied $N_\tau = 4$ extensively and demonstrated that it falls into the 3D Ising universality class. Their $N_s \to \infty$ estimate $\beta_c(4) = 2.29895\ (10)$ is marginally smaller than our estimate in Table I with $q = 0.042$ from a Gaussian difference test (see, e.g., [6]). For N_τ values up to $N_\tau = 8$ we found estimates in a paper by Lucini *et al.* [12]. Gaussian difference tests with our estimates give $q = 0.33$ and $q = 0.67$ for $N_\tau = 4$ and 6, respectively. For $N_\tau = 8$ their estimate $\beta_c(8) = 2.5090\ (6)$ is somewhat lower than ours of Table II, which has an error bar almost ten times smaller than theirs. The Gaussian difference test gives $q = 0.022$.

TABLE I. Pseudocritical β values N_s: β_c. Error bars of β_c are in parentheses.

$N_\tau = 4$	$N_\tau = 6$	$N_\tau = 8$
08: 2.30859 (53)	12: 2.43900 (33)	16: 2.52960 (90)
12: 2.30334 (33)	18: 2.43096 (43)	24: 2.51678 (43)
16: 2.30161 (30)	20: 2.42973 (11)	32: 2.51296 (20)
20: 2.30085 (17)	24: 2.42873 (35)	40: 2.51192 (12)
24: 2.30060 (16)	28: 2.427939 (74)	44: 2.51150 (11)
28: 2.30025 (19)	30: 2.427690 (87)	48: 2.51119 (11)
32: 2.299754 (99)	36: 2.427274 (67)	52: 2.51130 (11)
40: 2.299593 (74)	44: 2.426827 (67)	56: 2.511096 (85)
48: 2.299452 (83)	48: 2.426756 (64)	64: 2.510635 (83)
56: 2.299435 (29)	56: 2.426605 (62)	72: 2.510716 (72)
	60: 2.426596 (55)	80: 2.510517 (79)
∞: 2.299188 (61)	∞: 2.426366 (52)	∞: 2.510363 (71)
$q = 0.56$	$q = 0.73$	$q = 0.14$
$N_\tau = 4 \pm 0.00063$	$N_\tau = 6 \pm 0.0011$	$N_\tau = 8 \pm 0.0019$

For $N_\tau = 10$ and 12, calculations of the pseudocritical β values from maxima of the Polyakov loop susceptibility become very CPU time consuming. The largest statistics we assembled consists of slightly more than 2^{25} MCOR sweeps for the $40^3 12$ lattice. On even larger $N_\tau = 10$ and 12 lattices we spent 2^{23} MCOR sweeps. The largest amounts of CPU time were not spent on the largest lattices because we were mainly feeding on the NERSC scavenger queue. For comparison, at $\beta = 2.67$ we spent only 2^{19} MCOR sweeps on generating the 40^4 lattice used for the gradient flow. Taking achieved error bars, lattice sizes and

TABLE II. Pseudocritical β values N_s: β_c (continuation).

$N_\tau = 10$	$N_\tau = 12$
20: 2.59961 (52)	
24: 2.58909 (49)	24: 2.66317 (91)
28: 2.58497 (26)	
32: 2.58270 (27)	32: 2.64450 (39)
36: 2.58117 (13)	36: 2.64223 (33)
40: 2.58046 (26)	40: 2.64039 (26)
44: 2.58002 (17)	44: 2.63925 (24)
48: 2.57941 (15)	48: 2.63839 (27)
52: 2.57949 (23)	52: 2.63744 (19)
56: 2.57876 (18)	
64: 2.57851 (15)	
∞: 2.57826 (14)	∞: 2.63625 (35)
$q = 0.29$	$q = 0.06$
$N_\tau = 10 \pm 0.0045$	$N_\tau = 12 \pm 0.013$

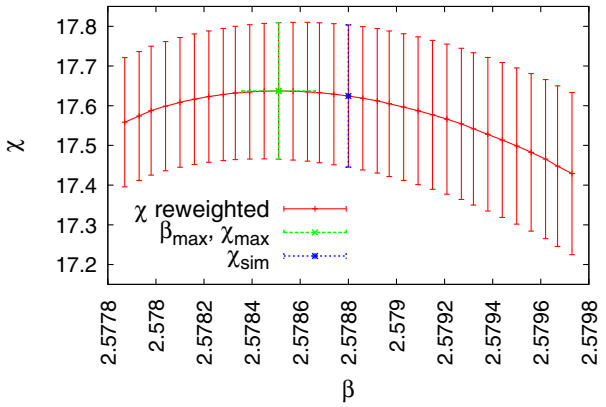

FIG. 1. Reweighting of the Polyakov loop susceptibility on our $64^3 10$ lattice.

numbers of lattices needed into account, this amounts to improvements by factors of at least 100. In view of the degrading of the deconfinement transition estimates with increasing lattice size, we also tried improved estimators [13], performing the SU(2) integration explicitly. However, correlations between Polyakov loops turned out to be too strong to allow for major gains.

For $N_\tau = 10$ and 12 the reweighting curve about the simulation point $\beta_{\rm sim}$ becomes rather flat within large error bars. See Fig. 1 for an example. Therefore, one may be amazed about the astonishingly accurate estimate of the maximum position $\beta_{\rm max}$. This is explained by the fact that all these error bars are strongly correlated, because they rely on reweighting of the same simulation. Dividing out the maximum value $\chi(\beta_{\rm max})$ of the susceptibility in each jackknife bin, one is led to Fig. 2, which projects out the central part around the maximum of the previous figure and makes the (jackknife) error bars of the $\beta_{\rm max}$ estimate plausible.

The scaling analysis of the $N_\tau(\beta_c)$ estimates of Tables I and II is performed in Sec. V.

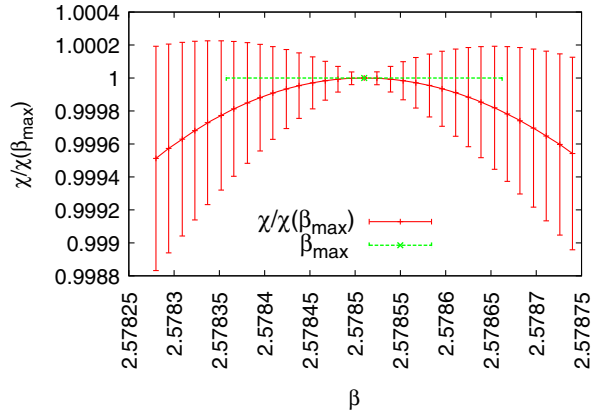

FIG. 2. Ratios of the Polyakov loop susceptibilities around the $\beta_{\rm max}$ value of our previous figure.

III. GRADIENT SCALE

Before coming to our central issue of scale setting we define the SU(2) gradient flow, the observables used and sketch our generation of MCMC data.

A. Gradient flow

With initial condition $U_\mu(n,0) = U_\mu(n)$ the gradient flow is defined [3] by the evolution equation

$$\dot{U}_\mu(n,t) = -g_0^2\{\partial_{n,\mu} S[U(t)]\}U_\mu(n,t). \tag{8}$$

Here the SU(2) link derivatives are given by

$$\partial_{n,\mu} f(U) = i\sum_{j=1}^{3}\sigma_j \frac{d}{ds} f(e^{isX^j}U)\big|_{s=0}, \tag{9}$$

where σ_j are the Pauli matrices and

$$X^j(m,\nu) = \begin{cases} \sigma^j & \text{if } (m,\nu) = (n,\mu), \\ 0 & \text{otherwise.} \end{cases} \tag{10}$$

We use the notation $U_\mu^{\square}$ for the sum of plaquette matrices containing the link matrix U_μ. With the definition of the staple matrix,

$$U_\mu^{\sqcup}(n) = \sum_{\nu\neq\mu} U_\nu(n)U_\mu(n+\hat{\nu})U_\nu^\dagger(n+\hat{\mu}) + \sum_{\nu\neq\mu} U_\nu^\dagger(n-\hat{\nu})U_\mu(n-\hat{\nu})U_\mu(n-\hat{\nu}+\hat{\mu}), \tag{11}$$

this is

$$U_\mu^{\square}(n) = U_\mu(n)U_\mu^{\sqcup}(n)^\dagger. \tag{12}$$

For the SU(2) link derivative (9) one finds the simple equation

$$g_0^2\partial_{n,\mu}S(U) = \frac{1}{2}(U_\mu^{\square}(n) - U_\mu^{\square}(n)^\dagger), \tag{13}$$

and we calculate the time evolution (8) using the Runge-Kutta scheme described in Appendix C of [3] with

$$Z_i = \epsilon Z(W_i), \qquad Z(W_i) = \frac{1}{2}(W_i - W_i^\dagger), \tag{14}$$

and $W_0 = U_\mu(n,t)$ as starting values and $\epsilon = 0.01$.

B. Observables

For the lattice expectation values of the time dependent plaquette matrices we use the parametrization

$$\langle U^{\square}(t)\rangle_L = a_0(t)\sigma_0 + i\sum_{i=1}^{3} a_i(t)\sigma_i, \tag{15}$$

where we suppress the $\mu\nu$ subscripts and σ_0 is the 2×2 unit matrix, supplementing the Pauli matrices σ_j. As observables we use three definitions of the energy density: $E_0(t)$, $E_1(t)$ and $E_4(t)$. Up to a constant factor

$$E_0(t) = 2[1 - a_0(t)] \tag{16}$$

is the usual Wilson action; i.e., it becomes $\sim F_{\alpha\beta}F_{\alpha\beta}$ in the continuum limit. The definition

$$E_1(t) = \sum_{i=1}^{3} a_i(t)^2 \tag{17}$$

has the same continuum limit as E_0. Finally, we denote by $E_4(t)$ Lüscher's [3] energy density which averages over the four plaquettes attached to each site n in a fixed $\mu\nu$, $\mu \neq \nu$ plane, i.e.,

$$\begin{aligned} E_4(t) &= \sum_{i=1}^{3} b_i(t)^2, \\ b_i(t) &= \frac{1}{4}(a_i^{ul} + a_i^{ur} + a_i^{dl} + a_i^{dr}), \end{aligned} \tag{18}$$

where the superscripts of a_i stand for up (u), left (l), right (r), and down (d) in a fixed $\mu\nu$ plane with respect to n (drawn in Fig. 1 of [3]). The functions

$$y_i(t) = t^2 E_i(t), \quad (i = 0, 1, 4) \tag{19}$$

are used to set the three gradient scales by choosing appropriate fixed values y_i^0 and iterating the time evolution (19) until

$$y_i^0 = (t_i^0)^2 E_i(t_i^0) \tag{20}$$

is reached. As a function of β the observable

$$s_i^0(\beta) = \sqrt{t_i^0(\beta)} \tag{21}$$

then scales like a length provided the following conditions are met:

(1) Lattice sizes have to be chosen so that $N_{\min} \gg \sqrt{8}s_i^0$ holds, where $\sqrt{8}s_i^0$ is the smoothing range [3] and $N_{\min} = \min\{N_i, i = 1, 2, 3, 4\}$ for simulations on a $N_1N_2N_3N_4$ lattice.
(2) The values of β have to be large enough to be in the SU(2) scaling region.
(3) The values of y_i^0 have to be large enough so that $\sqrt{8}s_i^0 \gg 1$ holds for the smallest used flow time.

C. Data generation and analysis

Our numerical results rely on MCMC simulations for the β values and lattice sizes given in Table V and (identically) in subsequent tables. In each run $128 = 2^7$ configurations were generated and on each of them the gradient flow was performed. To optimize our use of computational resources, we followed the rule of [6] and allocated our CPU time in approximately equal parts to the generation of configurations and to measurements (gradient flow). Subsequent configurations were separated by 2^{11} to 2^{13} MCOR sweeps where the increase from 2^{11} to larger numbers of MCOR sweeps is essentially enforced by the number of gradient sweeps needed to reach the y_i^0 target values. The dividing line from 2^{11} to 2^{12} sweeps is between $\beta = 2.574$ and $\beta = 2.62$, and from 2^{12} to 2^{13} between $\beta = 2.67$ and $\beta = 2.71$. We estimated integrated autocorrelation times τ_{int} with the software of [6] for the time series of 128 measured scale values and found all τ_{int} compatible with the lower bound 1, where the unit is set by the number of sweeps between the configurations.

In addition, we calculated the topological charge Q with the cooling method along the lines of Ref. [14]. The cooling method was introduced in Ref. [5] in the context of investigating the topological charge of the 2D O(3) sigma model. It has since then found many applications. For reviews see [15]. A SU(2) cooling update maps a link matrix

$$U_\mu(n) \to U'_\mu(n), \tag{22}$$

so that $U'_\mu(n)$ maximizes the local contribution to the action. This is achieved by

$$U'_\mu(n) = U^{\sqcup}_\mu(n)/\det|U^{\sqcup}_\mu(n)|, \tag{23}$$

where $U^{\sqcup}_\mu(n)$ is the staple matrix (11), which for SU(2) agrees up to the determinant factor with a SU(2) matrix.

We found that it takes for SU(2) about 100 cooling sweeps to reach reasonably long-lived metastable configurations and thus we decided to define the topological charge of a configuration by its value reached after 100 cooling sweeps. Figure 3 shows the cooling trajectories obtained from our 128 configurations at $\beta = 2.816$ on a 44^4 lattice with the corresponding histogram compiled in Table III.

To estimate topological correlations between our configurations we calculated the integrated autocorrelation times of the topological charge on our time series of 128 configurations. For our largest lattice at each β value the results are given in Table IV. Error bars are large as 128 data points is a rather small sample for calculating the integrated autocorrelation time. Within this limitation all values are compatible with 1. Statistical fluctuations allow for smaller values than this lower bound. When this

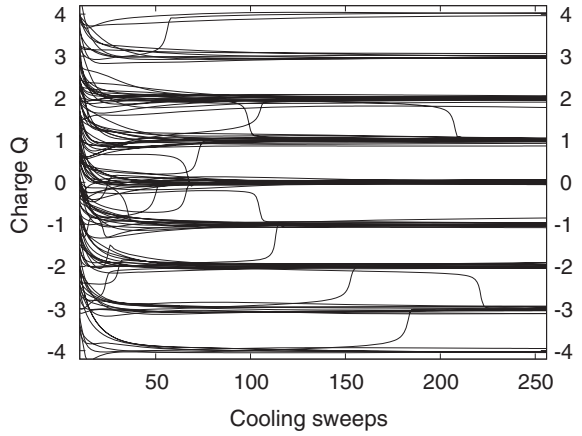

FIG. 3. Cooling of the topological charge on a 44^4 lattice at $\beta = 2.816$.

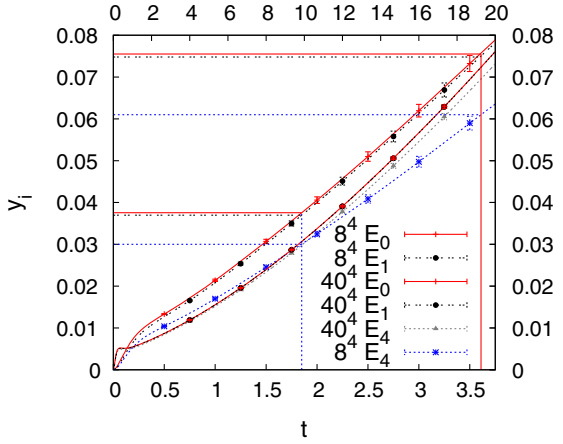

FIG. 4. Gradient flows $y_i(t)$ for the energy densities E_0, E_1 and E_4 at $\beta = 2.3$ on an 8^4 lattice (t on lower abscissa) and at $\beta = 2.574$ on a 40^4 lattice (t on upper abscissa). The up-down order in the legend agrees on the right-hand side with that of the curves.

happens the effective value at $t = 1$ is taken as the final estimate.

So, our data are considered to be statistically independent and error bars will be calculated by the jackknife method with respect to the 128 configurations. Mostly, we used N^4 lattices with the exception of $24^3 48$ and $32^3 64$, which mirror lattices used in [3]. The scale estimates from these asymmetric lattices are consistent with those we obtained from N^4 lattices.

D. Scale setting

From estimates of the deconfinement $\beta_c(N_\tau)$ values we know that it only makes sense to investigate SU(2) scaling for $\beta \geq 2.29$, $N_\tau \geq 4$. The smallest $N_s^3 4$ lattice size that can be used for the $N_\tau = 4$, $N_s \to \infty$ finite size extrapolation is given by $N_s = 8$. Therefore, it is natural to start our gradient flow simulations at $\beta = 2.3$ on an 8^4 lattice and to work from there up to larger β values and lattice sizes. It is of interest to control scaling violations at the lower end of the scaling region, because simulations there are less expensive than at larger β.

TABLE III. Histogram of the topological charge of Fig. 3 at 100 cooling sweeps.

−7	−6	−5	−4	−3	−2	−1	0	+1	+2	+3	+4	+5	+6	+7
0	1	0	6	11	16	17	24	21	19	8	3	0	1	1

TABLE IV. Integrated autocorrelation times of the topological charge.

β	Lattice	τ_{int}
2.3	16^4	1.26 (24)
2.51	28^4	1.01 (21)
2.574	40^4	1.49 (48)
2.62	40^4	0.91 (22)
2.674	40^4	0.92 (26)
2.71	40^4	0.85 (22)
2.751	40^4	1.68 (51)
2.816	44^4	1.59 (35)
2.875	52^4	1.17 (27)

The upper two curves (red, black) and the, ultimately, lowest (blue) curve of Fig. 4 show $y_i(t)$, ($i = 0, 1, 4$) from simulations on an 8^4 lattice (t on the lower abscissa). While the plots corresponding to E_0 and E_1 fall practically on top of one another, they deviate from the plot for E_4. This is due to finite lattice size corrections as well as scaling corrections in β. These corrections are much smaller for the other three curves which are from simulations at $\beta = 2.574$ on a 40^4 lattice. The corresponding t values are on the upper abscissa and chosen so that the largest y-values reached agree approximately with those from the 8^4 lattice.

The question is this: How does one pick a set of y_i^0 values that defines suitable s_i^0 scales according to Eqs. (20) and (21)? To minimize CPU time, one likes to keep the lattice size and s_0^i as small as possible. On the other hand, smaller s_0^i values imply larger discretization (finite lattice spacing) corrections and too small lattices imply finite size corrections. It is at this point that one encounters considerable ambiguities in the definition of gradient (and similarly cooling) scales.

In our context it is natural to define y_i^0 values so that our initial estimates from the s_i^0 scales are consistent with those from low $\beta_c(N_\tau)$ values. Lowest reasonable starting values for β, corresponding approximately to the $\beta_c(4)$ and $\beta_c(6)$ estimates of Table I, are $\beta_1 = 2.3$ and $\beta_2 = 2.43$. In Fig. 5 we plot ratio functions

$$\frac{s_i(N_2, \beta_2 = 2.43)}{s_i(N_1, \beta_1 = 2.3)}(y) \tag{24}$$

for $(N_2, N_1) = (12, 8)$ and (24,16). On the 1.5 line the outer curves correspond to (12,8) and the inner curves

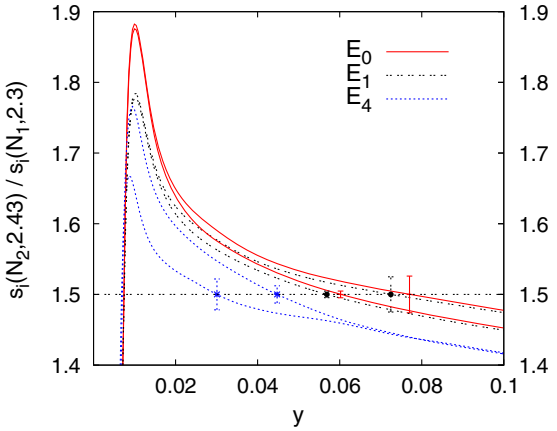

FIG. 5. Gradient flow ratios as functions of y. Outer curves: $s_i(12, 2.43)/s_i(8, 2.3)$. Inner curves: $s_i(24, 2.43)/s_i(16, 2.3)$.

(using the same colors) to (24,16). To prevent the figure from becoming too convoluted, error bars are only given on this line. As one expects from Fig. 4, the y values of the E_4 crossing points are apart from those of E_0 and E_1. The difference is considerably reduced when finite lattice size corrections are remediated by moving to (24, 16) lattices. The remaining difference should mainly be attributed to corrections in β (i.e., finite lattice spacing corrections).

One may have expected a plateau in the neighborhood of the 1.5 line, indicating that the ratios do not depend on the precise choice of the y_i^0 target values. Instead, without using the deconfinement result as input, another uncertainty in the choice of the y_i^0 target values would exist.

In the following we use the outer values of Fig. 5 and explore whether their differences result in seriously distinct scaling behavior. Starting off with $\beta = 2.3$, we are exploring two gradient scales:

(1) We define the y_i^{01} scale so that the E_4 observable delivers $s_4^{01}(12, 2.43)/s_4^{01}(8, 2.3) = 1.5$.
(2) We define the y_i^{02} scale so that for the E_i, $i = 0$, 1, observables $s_i^{02}(12, 2.43)/s_i^{02}(8, 2.3) = 1.5$ holds.

For the first case we find $y_4^{01} = 0.030$ from Fig. 5. Using $y_4(t)$ depicted in Fig. 4, $y_4^{01} = 0.030$ converts into the t value $t^{01} = 1.85$ for the flow time, as indicated by a vertical line. Its intersections with the $y_i(t)$ functions define our first set of y_i^0 target values

$$y_0^{01} = 0.0376, \quad y_1^{01} = 0.0370, \quad y_4^{01} = 0.030. \quad (25)$$

Similarly, our second set of y_i^0 values is derived from $t^{02} = 3.61$, which is the average value of t of the relevant crossing points of the E_0 and E_1 observables. This t^{02} value is also shown as a vertical line in Fig. 4 and leads to

$$y_0^{02} = 0.0755, \qquad y_1^{02} = 0.0748, \qquad y_4^{02} = 0.061. \quad (26)$$

Length scale values

TABLE V. Gradient length scale for the y_i^{01} set (25).

β	Lattice	$L_1 = s_0^{01}$	$L_2 = s_1^{01}$	$L_3 = s_4^{01}$
2.3	8^4	1.361 (13)	1.361 (13)	1.359 (15)
2.3	12^4	1.3538 (52)	1.3538 (50)	1.2955 (88)
2.3	16^4	1.3593 (28)	1.3589 (27)	1.2756 (75)
2.43	12^4	2.126 (20)	2.115 (20)	2.038 (20)
2.43	16^4	2.0961 (91)	2.0848 (90)	1.964 (14)
2.43	24^4	2.1066 (41)	2.0952 (40)	1.974 (11)
2.43	28^4	2.1023 (30)	2.0911 (30)	1.9666 (98)
2.51	16^4	2.730 (21)	2.715 (21)	2.603 (23)
2.51	20^4	2.766 (15)	2.750 (15)	2.585 (20)
2.51	28^4	2.7590 (73)	2.7428 (73)	2.570 (14)
2.574	20^4	3.389 (26)	3.369 (26)	3.166 (28)
2.574	24^4	3.395 (17)	3.374 (17)	3.175 (22)
2.574	32^4	3.406 (11)	3.385 (11)	3.193 (17)
2.574	40^4	3.4103 (72)	3.3896 (71)	3.149 (16)
2.62	24^4	3.993 (28)	3.968 (28)	3.711 (35)
2.62	$24^3 48$	3.947 (22)	3.923 (21)	3.699 (26)
2.62	28^4	3.950 (20)	3.926 (20)	3.704 (24)
2.62	40^4	3.954 (10)	3.9293 (99)	3.672 (19)
2.67	28^4	4.680 (33)	4.651 (33)	4.350 (39)
2.67	32^4	4.651 (27)	4.622 (27)	4.350 (33)
2.67	40^4	4.622 (17)	4.593 (17)	4.297 (24)
2.71	32^4	5.217 (37)	5.185 (37)	4.867 (42)
2.71	36^4	5.252 (33)	5.220 (33)	4.852 (42)
2.71	40^4	5.199 (22)	5.167 (22)	4.817 (27)
2.751	$32^3 64$	5.879 (35)	5.843 (34)	5.466 (39)
2.751	36^4	5.893 (38)	5.856 (38)	5.465 (48)
2.751	40^4	5.909 (34)	5.872 (34)	5.457 (41)
2.816	44^4	7.092 (48)	7.049 (47)	6.530 (54)
2.875	52^4	8.510 (64)	8.456 (65)	7.883 (68)

$$s_i^{0j}(\beta) = \sqrt{t_i^{0j}(\beta)}, \qquad i = 0, 1, 4, \qquad j = 1, 2 \quad (27)$$

are obtained when the gradient flow hits the corresponding y_i^{0j} definitions of Eqs. (25) or (26). Our MCMC estimates for them are reported in Tables V and VI. For later convenience we label the length scales by L_1 to L_6 as defined in the first row of the tables. We are led to $\sqrt{8t^{01}} \approx 3.85$ and $\sqrt{8t^{02}} \approx 5.37$ as our smallest values for the smoothing range. This is below and above the starting value $\sqrt{8t^0} \approx 4.77$ of Ref. [3] taken at $\beta = 5.96$ in the SU(3) scaling region. Comparing the SU(3) deconfinement transition values β_c for $N_\tau = 4$, 6, 8 (see, e.g., Ref. [16]) with those for SU(2) and performing interpolations of the β_c values, this corresponds roughly to $\beta = 2.46$ for SU(2), where our lower smoothing range has increased to at least 6.64. So, our lower smoothing range is also effectively larger than the one of [3].

TABLE VI. Gradient length scale for the y_i^{02} set (26).

β	Lattice	$L_4 = s_0^{02}$	$L_5 = s_1^{02}$	$L_6 = s_4^{02}$
2.3	8^4	1.897 (24)	1.897 (24)	1.900 (25)
2.3	12^4	1.8905 (84)	1.8897 (83)	1.824 (12)
2.3	16^4	1.8963 (48)	1.8956 (48)	1.807 (11)
2.43	12^4	2.849 (34)	2.842 (33)	2.771 (34)
2.43	16^4	2.791 (15)	2.784 (15)	2.653 (20)
2.43	24^4	2.8044 (66)	2.7968 (65)	2.644 (15)
2.43	28^4	2.7994 (48)	2.7920 (47)	2.645 (13)
2.51	16^4	3.586 (34)	3.575 (34)	3.436 (34)
2.51	20^4	3.653 (25)	3.642 (25)	3.453 (29)
2.51	28^4	3.624 (12)	3.613 (12)	3.406 (19)
2.574	20^4	4.437 (39)	4.423 (39)	4.178 (44)
2.574	24^4	4.429 (26)	4.415 (26)	4.171 (29)
2.574	32^4	4.454 (15)	4.440 (15)	4.219 (22)
2.574	40^4	4.458 (12)	4.444 (11)	4.175 (21)
2.62	24^4	5.252 (46)	5.233 (45)	4.916 (49)
2.62	$24^3 48$	5.135 (33)	5.119 (33)	4.868 (38)
2.62	28^4	5.145 (30)	5.129 (30)	4.849 (32)
2.62	40^4	5.156 (16)	5.140 (16)	4.827 (26)
2.67	28^4	6.131 (53)	6.110 (53)	5.740 (60)
2.67	32^4	6.057 (40)	6.038 (40)	5.719 (46)
2.67	40^4	6.020 (27)	6.000 (27)	5.645 (32)
2.71	32^4	6.776 (55)	6.754 (55)	6.357 (56)
2.71	36^4	6.831 (50)	6.809 (50)	6.401 (57)
2.71	40^4	6.773 (32)	6.751 (32)	6.334 (39)
2.751	$32^3 64$	7.642 (51)	7.617 (51)	7.179 (57)
2.751	36^4	7.659 (60)	7.633 (59)	7.161 (68)
2.751	40^4	7.694 (50)	7.668 (50)	7.211 (59)

For each β value several lattice sizes are listed in Tables V and VI to control finite size corrections. In most cases they are sufficiently weak to be swallowed by the statistical error bars. Exceptions are the s_4^{0j} estimates on 8^4 and 12^4 lattices at $\beta = 2.3$ and 2.43, which appear to be too small to accommodate E_4. Up to $\beta = 2.751$, lattices of size 40^4 appear to be large enough so that finite size corrections can be neglected. Larger lattices would just increase statistics due to self-averaging. For our largest lattices with $\beta = 2.816$ and 2.875 the gradient flow was designed too short to reach the y_i^{02} targets (26).

IV. COOLING SCALE

Our cooling sweeps are performed in the same systematic order as our MCMC sweeps.

Bonati and D'Elia [4] outlined that n_c cooling (22) sweeps correspond to a gradient flow time

$$t_c = n_c/3. \tag{28}$$

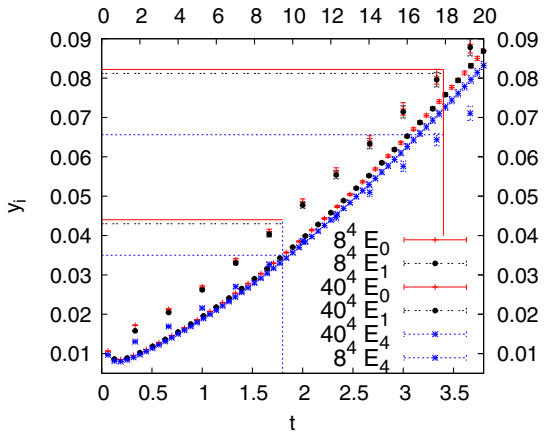

FIG. 6. Cooling flows $y_i(t)$ for the energy densities E_0, E_1 and E_4 at $\beta = 2.3$ on an 8^4 lattice (t on lower abscissa) and at $\beta = 2.574$ on a 40^4 lattice (t on upper abscissa).

TABLE VII. Cooling length scale for the y_i^{01} set (29).

β	Lattice	$L_7 = s_0^{01}$	$L_8 = s_1^{01}$	$L_9 = s_4^{01}$
2.3	8^4	1.342 (12)	1.337 (12)	1.342 (14)
2.3	12^4	1.3391 (47)	1.3343 (45)	1.2730 (85)
2.3	16^4	1.3433 (24)	1.3385 (23)	1.2575 (74)
2.43	12^4	2.111 (19)	2.092 (18)	2.013 (20)
2.43	16^4	2.0837 (90)	2.0653 (90)	1.951 (13)
2.43	24^4	2.0929 (38)	2.0744 (38)	1.947 (11)
2.43	28^4	2.0892 (28)	2.0707 (28)	1.9446 (95)
2.51	16^4	2.728 (19)	2.703 (19)	2.587 (23)
2.51	20^4	2.753 (14)	2.727 (14)	2.567 (20)
2.51	28^4	2.7522 (68)	2.7267 (66)	2.548 (15)
2.574	20^4	3.396 (25)	3.365 (24)	3.157 (26)
2.574	24^4	3.389 (16)	3.357 (16)	3.155 (22)
2.574	32^4	3.4001 (97)	3.3686 (95)	3.153 (17)
2.574	40^4	3.4048 (69)	3.3730 (67)	3.137 (17)
2.62	24^4	3.988 (26)	3.949 (26)	3.717 (32)
2.62	$24^3 48$	3.949 (20)	3.912 (19)	3.688 (25)
2.62	28^4	3.952 (19)	3.915 (19)	3.680 (23)
2.62	40^4	3.9509 (95)	3.9137 (93)	3.645 (22)
2.67	28^4	4.676 (32)	4.631 (31)	4.314 (39)
2.67	32^4	4.644 (27)	4.600 (26)	4.282 (31)
2.67	40^4	4.618 (17)	4.574 (16)	4.298 (26)
2.71	32^4	5.216 (36)	5.167 (35)	4.833 (41)
2.71	36^4	5.256 (31)	5.207 (31)	4.803 (42)
2.71	40^4	5.203 (21)	5.154 (21)	4.794 (28)
2.751	$32^3 64$	5.874 (32)	5.819 (32)	5.437 (37)
2.751	36^4	5.892 (36)	5.836 (35)	5.478 (49)
2.751	40^4	5.913 (32)	5.857 (32)	5.434 (40)
2.816	44^4	7.105 (45)	7.039 (45)	6.511 (55)
2.875	52^4	8.514 (60)	8.433 (59)	7.825 (68)

As we use $\epsilon = 0.01$ in our gradient flow steps, one cooling sweep corresponds to $33.\bar{3}$ gradient sweeps. On top of this (because of the Runge-Kutta), one gradient sweep demands more CPU time than one cooling sweep, so that the computational efficiency is improved by at least a factor of 34. *A priori* it is not obvious that many small gradient flow steps can be replaced by a large cooling step without losing accuracy of scale setting. *A posteriori* our results support that such a replacement is permissible.

Figure 6 is the analogue of Fig. 4. Due to the large cooling steps, gaps between them are clearly visible. They also exist in Fig. 4, but are there too small to be noticeable. Using linear interpolations, the crossing points of the ratio functions (24) determine initial scales for the cooling flow in precisely the same way as explained for the gradient flow. The values are summarized by the equations $t^{01} = 1.80$, $t^{02} = 3.40$,

$$y_0^{01} = 0.0440, \quad y_1^{01} = 0.0430, \quad y_4^{01} = 0.0350, \tag{29}$$

$$y_0^{02} = 0.0822, \quad y_1^{02} = 0.0812, \quad y_4^{02} = 0.0656. \tag{30}$$

The cooling scale $s_i^{0j}(\beta)$ values (27) are collected in Tables VII and VIII for the same lattices and β values as used for the gradient flow. For the analysis in the next section these length scales are labeled by L_7 to L_{12}. A detailed comparison of the scaling behavior of the deconfinement, gradient and cooling scales follows in the next section.

TABLE VIII. Cooling length scale for the y_i^{02} set (30).

β	Lattice	$L_{10} = s_0^{02}$	$L_{11} = s_1^{02}$	$L_{12} = s_4^{02}$
2.3	8^4	1.846 (22)	1.844 (22)	1.843 (22)
2.3	12^4	1.8241 (74)	1.8217 (72)	1.743 (12)
2.3	16^4	1.8307 (39)	1.8282 (39)	1.728 (10)
2.43	12^4	2.769 (29)	2.759 (29)	2.669 (32)
2.43	16^4	2.725 (14)	2.715 (14)	2.572 (18)
2.43	24^4	2.7395 (57)	2.7287 (57)	2.561 (14)
2.43	28^4	2.7317 (43)	2.7212 (42)	2.565 (12)
2.51	16^4	3.531 (30)	3.516 (30)	3.370 (31)
2.51	20^4	3.571 (23)	3.555 (23)	3.359 (27)
2.51	28^4	3.552 (10)	3.5371 (99)	3.315 (18)
2.574	20^4	4.356 (37)	4.337 (37)	4.084 (38)
2.574	24^4	4.352 (24)	4.333 (24)	4.080 (29)
2.574	32^4	4.374 (14)	4.355 (14)	4.100 (21)
2.574	40^4	4.377 (11)	4.358 (10)	4.074 (20)
2.62	24^4	5.157 (40)	5.133 (39)	4.836 (44)
2.62	$24^3 48$	5.070 (30)	5.047 (29)	4.788 (34)
2.62	28^4	5.059 (28)	5.037 (28)	4.751 (30)
2.62	40^4	5.068 (15)	5.045 (15)	4.725 (26)
2.67	28^4	6.021 (46)	5.993 (46)	5.603 (58)
2.67	32^4	5.950 (38)	5.923 (38)	5.532 (42)
2.67	40^4	5.910 (25)	5.884 (25)	5.536 (33)
2.71	32^4	6.656 (51)	6.626 (51)	6.208 (55)
2.71	36^4	6.724 (48)	6.692 (48)	6.223 (58)
2.71	40^4	6.656 (31)	6.626 (30)	6.188 (38)
2.751	$32^3 64$	7.515 (49)	7.481 (48)	7.010 (52)
2.751	36^4	7.531 (53)	7.497 (53)	7.033 (66)
2.751	40^4	7.576 (46)	7.541 (46)	7.038 (54)
2.816	44^4	9.056 (65)	9.015 (64)	8.349 (73)
2.875	52^4	10.879 (87)	10.830 (86)	10.122 (92)

V. SCALING AND ASYMPTOTIC SCALING

In this section we analyze scaling and asymptotic scaling for 13 length scales

$$L_k, \quad (k = 0, \ldots, 12) \tag{31}$$

defined as follows: the deconfining scale $L_0 = N_\tau(\beta_c)$ (4); six gradient length scales, $L_1, \ldots, L_6$; and six cooling length scales, $L_7, \ldots, L_{12}$. First, we consider $\mathcal{O}(a^2)$ scaling corrections for length ratios in the usual way (e.g., [3]). Then, we incorporate asymptotic scaling behavior along the lines of Refs. [17,18] and show how this can be done in a way consistent with $\mathcal{O}(a^2)$ scaling corrections.

A. Scaling

To compare mass or length scales it is customary to fit ratios to the linear form

$$R_{ij} = \frac{L_i}{L_j} = r_{ijk} + c_{ijk}\left(\frac{a}{l_k}\right)^2, \qquad l_k = aL_k, \tag{32}$$

where a is the lattice spacing; l_k the length scale in physical units; and r_{ijk}, c_{ijk} are fit parameters of which the r_{ijk} estimate the continuum limits and c_{ijk} the leading order corrections. We report in Table IX continuum estimates r_{ij} for the subset

TABLE IX. Estimates of r_{ij} ratios defined by Eq. (33).

$i\backslash j$	L_1	L_4	L_7	L_{10}
L_0	2.8896 (71)	2.2290 (46)	2.8855 (68)	2.2618 (42)
L_1	⋯	0.77382 (61)	0.99845 (38)	0.78433 (43)
L_3	0.9250 (19)	0.7163 (17)	0.9241 (19)	0.7264 (16)
L_4	1.2943 (11)	⋯	1.29135 (99)	1.01520 (49)
L_6	1.2090 (26)	0.9346 (20)	1.2081 (27)	0.9490 (21)
L_7	1.00156 (38)	0.77398 (79)	⋯	0.78570 (50)
L_9	0.9222 (21)	0.7141 (19)	0.9213 (20)	0.7243 (17)
L_{10}	1.27509 (70)	0.98508 (47)	1.27300 (80)	⋯
L_{12}	1.1835 (24)	0.9164 (21)	1.1825 (24)	0.9292 (19)

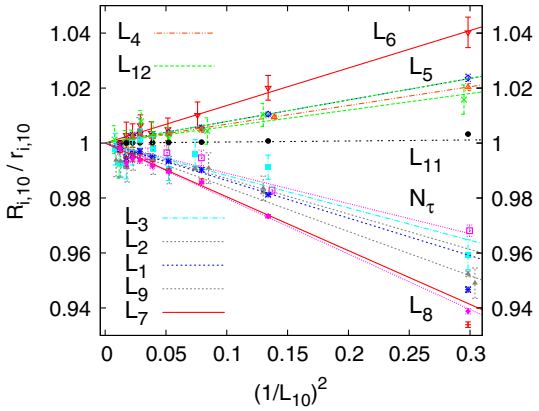

FIG. 7. Scaling corrections of order a^2 for ratios L_i/L_{10}. Here and in the next figures some data are slightly shifted for better visibility. To label all fits, some labels are attached to the lines and others put into the legend. The up-down order in the legend mirrors the up-down order in the plot.

$$R_{ij} = r_{ij} + c_{ij}\left(\frac{a}{l_j}\right)^2 = r_{ij} + c_{ij}\left(\frac{1}{L_j}\right)^2 \qquad (33)$$

with $i = 0, 1, 3, 4, 6, 7, 9, 10, 12$ and $j = 1, 4, 7, 10$. For $i \geq 1$ gradient and cooling scale fits, we use at each β value our largest lattice and R_{ij} error bars that rely on jackknife binning. In the case of the L_0 deconfinement scale, error propagation is used, where the values of the gradient and cooling scales at the β_c values are obtained by interpolating via an asymptotic scaling fit performed in the next subsection.

The scales L_2, L_5, L_8 and L_{11} are omitted from the table, because they rely on the E_1 energy definition, which agrees for practical purposes with E_0. For instance, $r_{11,10} = 0.995397(24)$, where the error bar is very small due to correlations between the E_0 and E_1 energy densities. Data points from $\beta = 2.3$ are eliminated from the fits for q values smaller than 0.05. After applying this cut, q was in the range 0.11 to 0.98.

To compare scaling corrections we divide the R_{ij} data by their continuum limits r_{ij} and choose as the reference scale $j = 10$ for reasons to be explained. A selection of the thus resulting fits is plotted in Fig. 7.

The fit for the deconfinement scale N_τ relies on the five β_c data points of Tables I, II and has a goodness of fit $q = 0.25$. The $q < 0.05$ cut was applied to the fits involving L_{11}, L_2, L_1 and L_7. For them deviations of the $\beta = 2.3$ data points from the fit lines are clearly visible in Fig. 7 at $(1/L_{10})^2 \approx 0.3$. The remaining seven fits include their $\beta = 2.3$ data points.

Essentially, the L_{11}/L_{10} fit takes on the constant value 1. Similarly, E_0, E_1 pairs stay together for the other scales. Generally, we notice that gradient and cooling scales that use the same energy observable and target value y_i^{01} or y_i^{02}

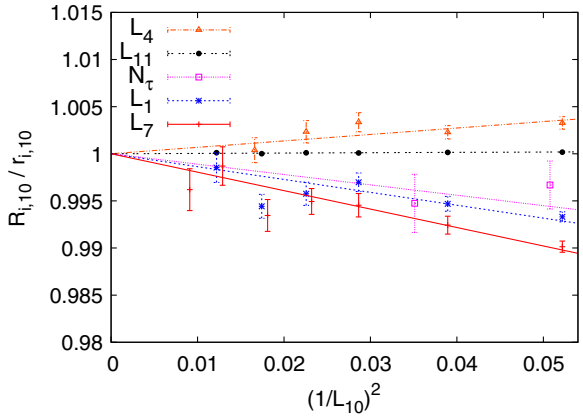

FIG. 8. Enlargement of the continuum approach of Fig. 7 for the E_0, the L_{11} and the deconfinement scales.

stay closer together than gradient scales using different energy observables and target values or cooling scales using different energy observables and target values. The ratios of Table IX show the same pattern. So, it appears perfectly legitimate to use cooling instead of gradient scales. We opted for L_{10} as the reference scale, because it centers rather nicely with respect to the other scales. At $(1/L_{10})^2 \approx 0.3$ in Fig. 7 we read off scaling violations of about 10%, i.e., 0.94 to 1.04 for $R_{i,10}/r_{i,10}$. That is larger than the 5% reported by Lüscher [3] in his Fig. 3 for SU(3) at $\beta = 5.96$. As outlined, this corresponds to $\beta \approx 2.46$ for SU(2), which translates into $(1/L_{10})^2 \approx 0.11$. In Fig. 7 this is slightly left of the column of data at $(1/L_{10})^2 \approx 0.13$ for which we find the range $0.97 < R_{i,10}/r_{i,10} < 1.02$; i.e., scaling violations are down to less than 5%.

A problem with plots like Fig. 7 is that data from large lattices (close to the continuum limit) accumulate in a small region, which is here below $(1/L_{10})^2 < 0.05$. It is enlarged in Figs. 8 and 9. In Fig. 9 the length scales based on the E_4 energy are plotted and seen to exhibit considerably larger

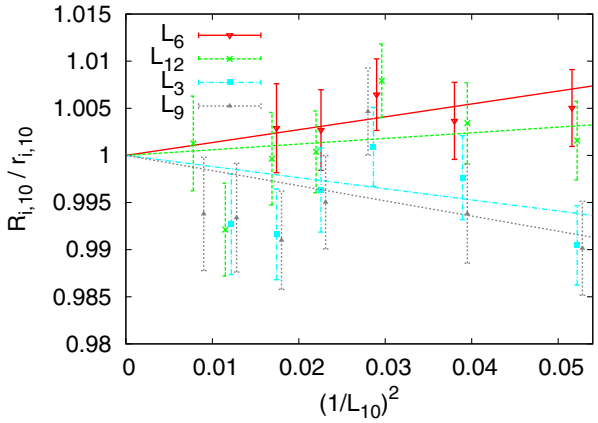

FIG. 9. Enlargement of the continuum approach of Fig. 7 for the E_4 scales.

error bars than the energy scales plotted in Fig. 8. With no particular advantages to offset this lack of accuracy of the E_4 scales, all arguments converge in favor of using an E_0 cooling scale.

B. Asymptotic scaling

For large β the scaling of any mass m in pure SU(N) LGT is determined by the asymptotic scaling function

$$\begin{aligned} am &= \text{const} f_{as}(\beta), \\ f_{as}(\beta) &= \alpha a \Lambda_L = \alpha \left(b_0 \frac{2N}{\beta} \right)^{-b_1/2b_0^2} \\ &\quad \times \exp\left(-\frac{\beta}{4Nb_0} \right) \left[1 + \sum_{j=1}^{\infty} q_j \left(\frac{2N}{\beta} \right)^j \right], \end{aligned} \tag{34}$$

where a is the lattice spacing, and $b_0 = 11N/(48\pi^2)$ and $b_1 = (34/3)N^2/(16\pi^2)^2$ are, respectively, the universal 1-loop [19,20] and 2-loop [21,22] asymptotic scaling coefficients. Universal means that all renormalization schemes lead to the same b_0 and b_1 values. Nonuniversal perturbative corrections are given by the q_j coefficients in the bracket. Computing up to 3 loops, Allés *et al.* [23] calculated q_1 for SU(N) LGT and

$$q_1 = 0.08324 \quad \text{for SU(2)}. \tag{35}$$

Further, we introduce the factor α to enforce for SU(2) the convenient normalization

$$f_{as}(2.3) = 1. \tag{36}$$

Higher order corrections in the lattice spacing a are reflected by terms of the form

$$(\alpha a \Lambda_L)^i = [f_{\text{as}}(\beta)]^i, \quad (i = 2, 3, \ldots). \tag{37}$$

Following Allton [17] in the version of [18] we arrive at the expansions

$$L_k = \frac{c_k}{f_{as}(\beta)} \left(1 + \sum_{i=1}^{\infty} a_k^i [f_{as}(\beta)]^i \right) \tag{38}$$

for our length scales, where c_k and the a_k^i are parameters that have to be calculated. In practice we have to truncate the series (38) as well as the definition (34) of $f_{as}(\beta)$. Defining

$$f_{as}^0(\beta) = \alpha^0 \left(b_0 \frac{2N}{\beta} \right)^{-b_1/2b_0^2} \exp\left(-\frac{\beta}{4Nb_0} \right), \tag{39}$$

$$f_{as}^1(\beta) = \left(\frac{\alpha^1}{\alpha^0} \right) f_{as}^0(\beta) \left(1 + \frac{4q_1}{\beta} \right), \tag{40}$$

we have f_{as}^m with $m = 0$, 1 at our disposal, where the coefficients α^m are defined to enforce as in (36) the normalizations $f_{as}^m(2.3) = 1$. Truncating the sum (38) by fixed n, we end up with 26 fits ($k = 0, \ldots, 12$), ($m = 0$, 1):

$$L_k^{m,n} = \frac{c_k^{m,n}}{f_{as}^m(\beta)} \left(1 + \sum_{i=1}^{n} a_k^{m,i} [f_{as}^m(\beta)]^i \right), \tag{41}$$

where the index n of $a_k^{m,i}$ is suppressed. Due to the truncation of f_{as} there are perturbative corrections in $1/\beta$ when ratios are taken with respect to the (inverse) lambda lattice scale; i.e.,

$$L_k^{m,n} \alpha^m a \Lambda_L = c_k^{m,n} + \text{perturbative corrections} \tag{42}$$

describes asymptotic scaling. Corrections to ratios of two length scales are exponentially small in β; i.e.,

$$\frac{L_{k_1}^{m,n_1}}{L_{k_2}^{m,n_2}} = \frac{c_{k_1}^{m,n_1}}{c_{k_2}^{m,n_2}} + \text{nonperturbative corrections} \tag{43}$$

holds. However, due to the $a_k^{m,1}$ term in (41), corrections would in general be of order a in the lattice spacing and not of order a^2 as in (33). In [18] this problem was avoided by combining several scales into one fit. This is only possible when their relative scaling violations are so weak that they become invisible within statistical errors. The solution which we propose here is to fit all $k = 0, 1, \ldots, 12$ scales with identical $a_k^{m,1}$ coefficients so that the nonperturbative corrections (43) become $\mathcal{O}(a^2)$.

Estimates of normalization constants for asymptotic scaling fits are collected in Table X. As before, the gradient and cooling scale fits use our largest lattice at each β value. The last row of the table gives the $a_k^{m,1}$ values taken for all fits of their respective columns. Using the E_0 and E_4 scales these values were determined by the maximum likelihood method (E_1 scales are left out because they would in essence amplify weights of the E_0 scales). On a technical note, we remark that we eliminate the normalization constants $c_k^{m,n}$ from the search for the χ^2 minimum by treating them as functions of the $a_k^{m,i}$ parameters [24]. This stabilizes the search considerably, for which we used the Levenberg-Marquardt approach (e.g., [6]).

Fitting the gradient and cooling scales ($k \geq 1$) with only one additional parameter, $a_k^{1,2}$, the normalization constants $c_k^{1,2}$ of column 2 are obtained. Most q values of these fits are too low. So, we decided to allow for one more fit parameter, $a_k^{m,3}$. The results are shown in columns four and six (using f_{as}^m with $m = 0$, 1). Now, the q values for these fits would be too good to be true if they were statistically independent.

TABLE X. Asymptotic scaling fits of normalization constants and goodness of fit q.

k	$c_k^{1,3}$	q	$c_k^{0,4}$	q	$c_k^{1,4}$	q
0	6.6682 (56)	0.00	6.114 (29)	0.71	5.892 (27)	0.68
	$c_k^{1,2}$		$c_k^{0,3}$		$c_k^{1,3}$	
1	2.2481 (32)	0.04	2.1937 (64)	0.91	2.1083 (61)	0.91
2	2.2311 (32)	0.03	2.1812 (64)	0.92	2.0961 (60)	0.92
3	2.0743 (56)	0.17	2.022 (11)	0.66	1.9432 (98)	0.67
4	2.8945 (54)	0.08	2.846 (11)	0.98	2.735 (11)	0.98
5	2.8835 (53)	0.04	2.837 (11)	0.98	2.727 (11)	0.98
6	2.7068 (85)	0.95	2.658 (18)	0.95	2.555 (17)	0.95
7	2.2498 (30)	0.02	2.1996 (61)	0.93	2.1138 (57)	0.94
8	2.2254 (30)	0.01	2.1807 (60)	0.92	2.0956 (57)	0.93
9	2.0664 (58)	0.16	2.018 (11)	0.69	1.9397 (99)	0.69
10	2.8501 (46)	0.02	2.8037 (91)	0.89	2.6942 (86)	0.89
11	2.8357 (45)	0.01	2.7914 (89)	0.88	2.6824 (85)	0.89
12	2.6485 (74)	0.26	2.599 (14)	0.52	2.498 (13)	0.52
	$a_k^{1,1} = -0.6209$		$a_k^{0,1} = -0.38157$		$a_k^{1,1} = -0.32536$	

As they all rely on the same data set correlations can explain that a whole series of fits exhibits $q > 0.5$, mostly close to 0.9. Notably, consistent fits due to adding the $a_k^{m,3}$ parameters come at the price of about doubled error bars compared to those of column two.

It is possible to include the deconfinement length scale into these fits with fixed $a_k^{m,1}$ and the results are given in the second row of Table X. Despite the small number of only five data points (Tables I and II) one needs one more parameter, $a_0^{m,4}$, to get acceptable q values. This is accompanied by some instability discussed at the end of this section.

Using the f_{as}^1 instead of the f_{as}^0 asymptotic scaling function decreases all c_k values by slightly less than 4%. More prominent is the decrease between 6.7% and 9% from column 2 to column 6 of Table X, which comes from allowing one more free parameter. Together we take this as an indication that the remaining systematic errors may well reach 10%.

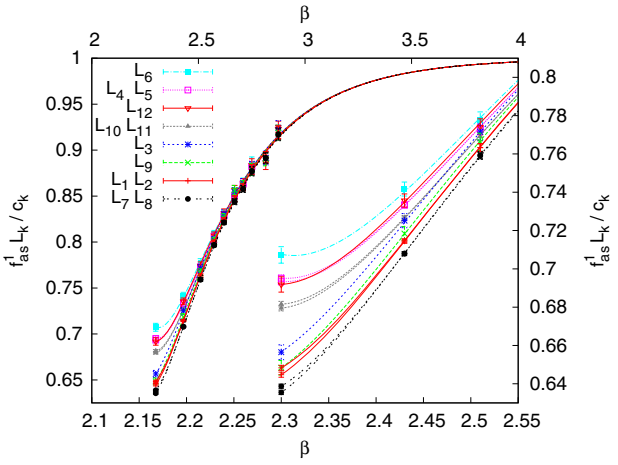

FIG. 10. Asymptotic scaling.

Dividing out the asymptotic scaling behavior $c_k^{1,n}/f_{as}^1(\beta)$, we plot in Fig. 10 the resulting fits $f_{as}^1 L_k^{1,3}/c_k^{1,3}$ $(k \geq 1)$ for column 6 of Table X. For the curves on the left the abscissa is on top of the figure and the ordinate on the left. At $\beta = 4$ all fits have almost reached the asymptotic value 1. The lower abscissa and the right ordinate apply to the right part of Fig. 10, which enlarges the range of our initial three β values. At $\beta = 2.3$ asymptotic scaling violations are seen to range from 28% to 37%. The relative differences reach only $0.72/0.63 \approx 1.14$, consistent with the ratio $1.04/0.93 \approx 1.12$ observed at $(1/L_{10})^2 = 0.3$ in Fig. 7.

Let us turn to the scaling behavior of ratios. Except for the deconfinement length scale L_0, which is statistically independent from the other scales, we cannot use error propagation. Instead, we calculate the R_{ij} ratios (33) for jackknife bins built from the individual gradient or cooling flow runs (using jackknife bins of the asymptotic scaling fits of Table X has the problem that these fits have larger fluctuations than the R_{ij} ratios).

For $m = 1$ results are collected in Table XI. With the exception of the L_0 (as) row (to be discussed) all fits use

$$a_k^{1,1} = 0 \tag{44}$$

to reflect that the leading scaling corrections for mass ratios are $\mathcal{O}(a^2)$. We end up with

$$R_{ij} = r_{ij} + \sum_{i=2}^{n} a^{1,i} [f_{as}^1]^i. \tag{45}$$

Surprisingly, one additional free parameter $a_k^{1,2}$, besides the ratio estimate r_{ij}, gives in more than half of the cases a

TABLE XI. Estimates of r_{ij} ratios from scaling fits of jackknifed R_{ij} data.

$i\backslash j$	L_1	L_4	L_7	L_{10}
L_0 (as)	2.795 (16)	2.154 (14)	2.787 (15)	2.187 (13)
L_0	*2.914 (15)	2.2393 (52)	*2.903 (14)	2.2692 (48)
L_1	...	*0.7703 (12)	0.99808 (34)	*0.78185 (77)
L_3	0.9240 (20)	0.7187 (19)	0.9221 (20)	0.7275 (17)
L_4	*1.2996 (21)	...	*1.2957 (27)	1.01373 (57)
L_6	1.2000 (31)	0.9334 (23)	1.1972 (32)	0.9465 (24)
L_7	1.00188 (34)	*0.7728 (16)	...	*0.78419 (88)
L_9	0.9214 (22)	0.7171 (21)	0.9197 (22)	0.7255 (18)
L_{10}	*1.2795 (13)	0.98638 (55)	*1.2760 (15)	...
L_{12}	1.1786 (26)	0.9167 (24)	1.1760 (26)	0.9283 (20)

satisfying goodness of fit ($0.13 \leq q \leq 0.99$). For the other cases, indicated by * in Table XI, the parameter $a_k^{1,3}$ is also needed ($0.45 \leq q \leq 0.75$ holds for these). Comparing with our previous ratio estimates of Table IX, we see that the error bars of the starred estimates are about two times larger, while the error bars of the other estimates are similar as before. Systematic errors due to the different fits are around 1%, which is up to an order of magnitude larger than the statistical errors. The latter can be extremely small due to correlations between the estimators.

Using the asymptotic scaling function with $m = 0$ instead of $m = 1$, differences for ratios are about 2 orders of magnitude smaller than those encountered for the normalization constants of Table X. Asymptotic scaling corrections drop out, as one expects. The systematic error due to adding the $a_k^{m,3}$ fit parameter can be considerably larger, up to 1.3%. This is still about 1 magnitude smaller than the same systematic uncertainty in the case of the normalization constants.

Dividing the constants r_{ij} out, Figs. 11 and 12 give a visual impression of the scaling of selected fitting curves with reference scale L_{10}. Superficially, curves for the same scales look similar in Fig. 12 as before in Figs. 8 and 9.

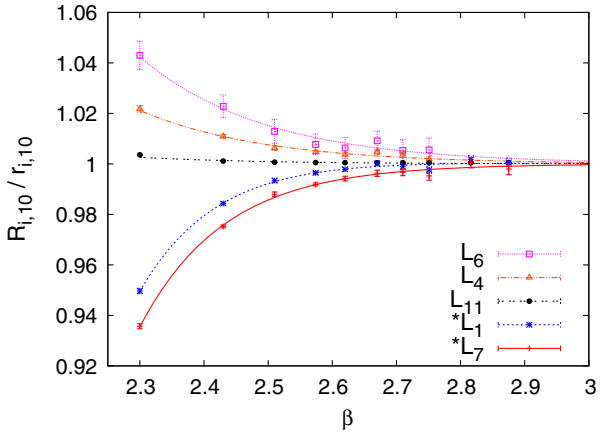

FIG. 11. Scaling corrections of the E_0, the L_{11} and the deconfinement scale ratios with respect to L_{10}.

However, there is a fundamental difference between the fits. Equation (45) ensures that $L_i/L_{10} \sim (1/L_{10})^2$ is correct in the limit $(1/L_{10})^2 \to 0$, while in Eq. (33) it is assumed to be already exact for the data at hand. Now, for the fits (45) the straight line behavior is in some cases only reached for very small $(1/L_{10})^2$. This is most pronounced for the $R_{1,10}/r_{1,10}$ fit, which crosses the value 1 from below and finally approaches 1 from above, once the region $(1/L_{10})^2 < 0.005$ on the very left side of Fig. 12 is reached (details are not visible on the scale of the figure). In view of this it is reassuring that the estimates of Tables IX and XI never differ by more than 1.3%. The two fitting approaches supplement one another and give some insight into the systematic errors one may expect.

We conclude this section by discussing the instabilities encountered when fitting L_0/L_i. In the L_0 (as) row of Table XI we report estimates obtained from using the constants of column 6 of Table X and error propagation. Compared with the previous estimates of Table IX we find a systematic decrease in the range 3.2% to 3.6%, larger than the statistical error, which never exceeds 0.6%. As the asymptotic scaling of L_0 needs four parameters to fit just five data points one may suspect "overfitting." As a tiebreaker we perform the fit of Eq. (45) for jackknifed ratios of L_0/L_j, $j = 1, 4, 7, 10$, and obtain the estimates of

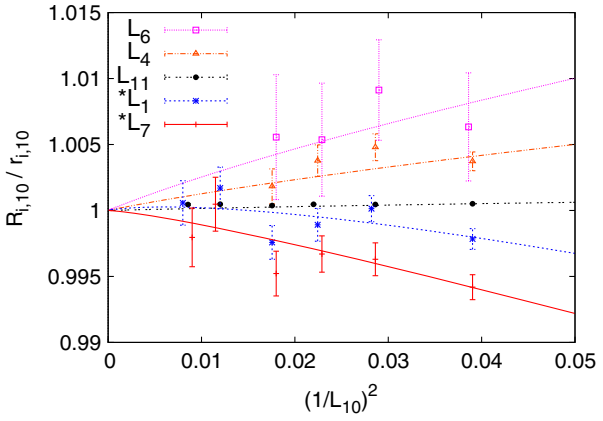

FIG. 12. Figure 11 plotted in the $(1/L_{10})^2$ range of Fig. 8.

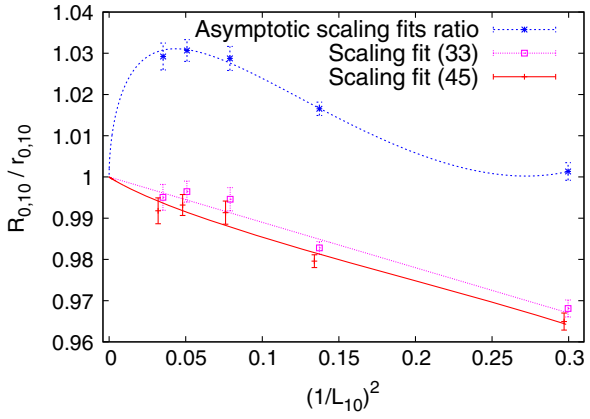

FIG. 13. Three fits of the deconfinement length scale L_0 versus $(1/L_{10})^2$.

the L_0 row of Table XI. The systematic errors with respect to Table IX are now down to less than 1%.

Dividing the asymptotic ratios out, the three fits for L_0/L_{10} are shown in Fig. 13. The straight line fit from Figs. 7 and 8 comes in as the second lowest. The lowest curve corresponds to Eq. (45) and the upper curve to dividing the L_0 fit of column 6 of Table X by the L_{10} fit of the same column. As suspected this curve looks rather fanciful. However, using a log scale for the abscissa would stretch the range on the left, and one should keep in mind that the absolute differences among all three fits are quite small. Systematic errors at $(1/L_{10})^2 = 0.3$ can be read off on the right-hand side of the figure and are seen to be less than 4%.

VI. SUMMARY AND CONCLUSIONS

We have studied the approach of SU(2) LGT to its quantum continuum limit by investigating the scaling behavior of a number of length scales with definitions based on the deconfinement phase transition, the gradient flow and the cooling flow. While the deconfining scale $L_0 = N_\tau$ is uniquely defined (4), one has considerable freedom in the definition of gradient and cooling flow scales. They depend on the choice of observables and target values of the flow. We considered the following:

(1) Energy densities E_0, E_1, E_4 defined by Eqs. (16), (17), and (18). E_0 is up to normalization the Wilson action and E_1 is in essence an equivalent definition. E_4, introduced in [3], averages over four plaquettes.
(2) Target values y_i^{01} and y_i^{02} ($i = 0, 1, 4$) are defined by Eqs. (25), (26), (29), and (30). They are constructed so that the initial scaling behavior of either the gradient or the cooling flow of E_0, E_1 or E_4 matches that of the deconfinement length N_τ (altogether $3 \times 4 = 12$ distinct definitions).

For ratios of these length scales, corrections to scaling are supposed to be of order a^2 in the lattice spacing as illustrated in Figs. 7, 8, 9, 12 and 13. In these figures the cooling length scale L_{10}, which relies on the E_0 energy density and a y_0^{02} target value (30), is used as a reference scale for the following reasons:

(1) Scaling violations of ratios of scales are then rather symmetrically distributed above and below 1.
(2) E_0 is easier to calculate than E_4 and estimates from the same statistics result in smaller error bars for the E_0 length scale. No scaling advantages were found for E_4 scales. E_1 is essentially equivalent to E_0 with the benefit for E_0 that the Wilson action is implemented in the program anyhow.
(3) The cooling flow is faster and easier to calculate than the gradient flow and there is no noticeable loss of accuracy as anticipated in Ref. [4]. As the cooling method [5] was an answer to difficulties encountered when trying to calculate the topological charge in a paper by Lüscher and one of the authors [25], it appears that the cooling scale could have been introduced 30 years before the gradient scale [3].

The magnitude of scaling violations we find for ratios of length scales is close to that reported in Ref. [3] for SU(3) when comparing the E_0 with the E_4 flow. The SU(2) scaling region begins at $\beta = 2.3$ where we find corrections to scaling in the 10% range. Deeper in the scaling region, at $\beta = 2.46$, they become reduced to slightly less than 5%.

Scaling corrections for the ratio N_τ/L_{10} fall into the range provided by the other scales as is seen in Figs. 7 and 8. The significant advantage of the gradient scale, and to an even greater extent the cooling scale, over the deconfinement scale is that we can far more easily follow the scaling behavior towards the continuum limit. On the other hand, there are no ambiguities in the definition of the deconfinement scale, which makes it kind of ideal to define initial scaling values as discussed in Secs. III and IV.

We have used two rather different approaches for analyzing our data. For Figs. 7 to 9 we simply calculate L_i/L_{10} from jackknife bins of the data and perform the linear two-parameter fit (33) using the $\mathcal{O}(a^2)$ dependence $(1/L_{10})^2$ from the same data. While this is straightforward, one does not connect with the asymptotic Λ_L scale.

To connect with asymptotic scaling, we relied on truncated forms of Eq. (34) based on Refs. [17,18]. The normalization constants of our asymptotic scaling fits are collected in Table X. A common fixed parameter ensures that scaling corrections for ratios are $\mathcal{O}(a^2)$. Systematic errors due to distinct truncations of the fits are found around 10%. For the gradient and cooling scales the finally accepted fits of column 6 rely on three free parameters, one of them being the normalization constant that yields the continuum estimate. For L_0 four fit parameters are needed despite the fact that there are only five data points. Comparing in Fig. 13 the ratio of the L_0 and L_{10} fit with direct fits of the $R_{0,10}$ ratios indicates overfitting, though L_0 data on larger lattices are needed to be conclusive.

While the lattice spacing is exponentially small in β, asymptotic scaling corrections come in powers of $1/\beta$. As is

seen in Fig. 10, they range at $\beta = 2.3$ from 30% to 36%. The scales cluster together, so that the relative deviations at $\beta = 2.3$ reproduce the previously encountered 10% range.

For ratio estimates it turns out that one should not divide the asymptotic scaling estimates by one another, but perform the fit (45) for the jackknifed R_{ij} ratios of the data, where the common fixed parameter is set to zero to enforce $\mathcal{O}(a^2)$ corrections. A decisive difference to the previous approach (33) remains: the $\mathcal{O}(a^2)$ behavior is no longer enforced for our data at hand, but only in the continuum limit. Indeed, some of the fits make use of this possibility. Compare Fig. 12 with Figs. 8 and 9. Despite the differences in the approach to the continuum limit, the obtained curves look similar.

The continuum limit estimates of our ratios are collected in Tables IX and XI using, respectively, (33) and (45). Differences due to the distinct fit forms stay below 1.3%. This is in most cases larger than the statistical errors. The different fit forms allow one to get an idea of the systematic errors possible.

In conclusion, we hope that the methods outlined are also of some value for studying the approach of physically realistic theories like QCD to their continuum limits. Though such data rely on large scale calculations on supercomputers, it is presumably safe to assume that their quality is not better than that of our SU(2) data. Therefore, our results can be seen as a warning that one needs simulations rather deep in the scaling region to achieve an accuracy of about 1% scaling violations. Besides statistical errors we find systematic uncertainties which can easily outweigh them.

ACKNOWLEDGMENTS

D. C. was in part supported by the U.S. Department of Energy (DOE) under Contract No. DE-SC0010102. Our calculations used resources of the National Energy Research Scientific Computing Center (NERSC), a DOE Office of Science User Facility supported by the DOE under Contract No. DE-AC02-05CH11231.

[1] Z. Fodor and C. Hoelbling, Rev. Mod. Phys. **84**, 449 (2012); C. Liu, *Proc. Sci.* Lattice 2016 (2016) 006.
[2] B. Svetisky and G. Yaffe, Nucl. Phys. **B210**, 423 (1982).
[3] M. Lüscher, J. High Energy Phys. 08 (2010) 071; 03 (2014) 092(E).
[4] C. Bonati and M. D'Elia, Phys. Rev. D **89**, 105005 (2014).
[5] B. A. Berg, Phys. Lett. **104B**, 475 (1981).
[6] B. A. Berg, *Markov Chain Monte Carlo Simulations and Their Statistical Analysis* (World Scientific, Singapore, 2004).
[7] K. Fabricius and O. Haan, Phys. Lett. **143B**, 459 (1984); A. D. Kennedy and B. J. Pendleton, Phys. Lett. **156B**, 393 (1985).
[8] S. L. Adler, Phys. Rev. D **37**, 458 (1988).
[9] D. Barkai and K. J. M. Moriarty, Comput. Phys. Commun. **27**, 105 (1982).
[10] B. A. Berg and Hao Wu, Comput. Phys. Commun. **183**, 2145 (2012).
[11] J. Engels, S. Mashkevich, T. Scheideler, and G. Zinovjec, Phys. Lett. B **365**, 219 (1996); J. Engels and T. Scheideler, Nucl. Phys. **B539**, 557 (1999).
[12] B. Lucini, M. Teper, and U. Wenger, J. High Energy Phys. 01 (2004) 061.
[13] G. Parisi, R. Petronzio, and F. Rapuano, Phys. Lett. **128B**, 418 (1983).
[14] L. Del Debbio, H. Panagopoulos, and E. Vicari, J. High Energy Phys. 08 (2002) 044.
[15] J. Negele, Nucl. Phys. B, Proc. Suppl. **73**, 92 (1999); E. Vicari and H. Panagopoulos, Phys. Rep. **470**, 93 (2009).
[16] A. Francis, O. Kaczmarek, M. Laine, T. Neuhaus, and H. Ohno, Phys. Rev. D **91**, 096002 (2015).
[17] C. R. Allton, Nucl. Phys. B, Proc. Suppl. **53**, 867 (1997).
[18] B. A. Berg, Phys. Rev. D **92**, 054501 (2015).
[19] D. J. Gross and F. Wilczek, Phys. Rev. Lett. **30**, 1343 (1973).
[20] H. D. Politzer, Phys. Rev. Lett. **30**, 1346 (1973).
[21] D. R. T. Jones, Nucl. Phys. **B75**, 531 (1974).
[22] W. Caswell, Phys. Rev. Lett. **33**, 244 (1974).
[23] B. Allés, A. Feo, and H. Panagopoulos, Nucl. Phys. **B491**, 498 (1997).
[24] B. A. Berg, Comput. Phys. Commun. **200**, 254 (2016); **208**, 169(E) (2016); G. H. Golub and V. Pereya, SIAM J. Numer. Anal. **2**, 413 (1972).
[25] B. A. Berg and M. Lüscher, Nucl. Phys. **B190**, 412 (1981).